Original Article

Received: 2024-10-12
Accepted: 2024-12-08

BCCR
2024, No 4, Vol 16 :196-215
www.bccrjournal.com

http://doi.org/10.18502/bccr.v16i4.20861

Proton Beam Physical Processes for Improving Cancer Therapy Using a Water Phantom

Fatemeh Namdari, Seyede Nasrin Hosseinimotlagh[1*]

1

Department of Physics, Shi.C., Islamic Azad University, Shiraz, Iran

*Corresponding Author:
Seyede Nasrin Hosseinimotlagh
Department of Physics, Shi.C., Islamic Azad University, Shiraz, Iran

Email: nasrinhosseini_ motlagh@iau.ir

ABSTRACT

Proton beam radiation offers improved cancer therapy due to its unique physical properties, particularly the Bragg peak, which allows for precise energy deposition within the tumor while minimizing damage to surrounding healthy tissue. This is especially beneficial when treating tumors near sensitive organs. Water is frequently used as a reference medium for calculating and measuring proton beam properties like range and dose, as it closely mimics human tissue in terms of energy loss and scattering. The goal of this work is to describe quantitatively and qualitatively physical processes using both Maple programming and GEANT4 simulation for proton treatment when a proton pencil beam passes through a water phantom.

Keywords:Bragg Peak; Proton Treatment; Radiotherapy; Depth-Dose; Cross-Section

INTRODUCTION:

One of the most important types of cancer treatments to control cancer cells is radiotherapy. Radiotherapy is a standard treatment option used for 50–75% of cancer patients [1–3]. Over recent decades, proton therapy has seen significant technological advancements and increased clinical applications [4, 5]. The proton beam is characterized by its Bragg peak, which has a sharp dose fall-off after the target. This characteristic allows proton therapy to achieve improved dose conformality to the target and enhanced dose protection to organs at risk compared to conventional photon therapy [6–13].
Despite the dosimetric benefits, proton therapy faces a major challenge in accurately modeling and understanding the relative biological effectiveness [14–19]. In contrast to photons, protons impart most of their energy over a short distance and thus, induce high linear energy transfer near the distal end of the Bragg Peak. Hence, the biological effect of proton therapy should be determined by both dose and linear energy transfer (and possibly other factors) [14, 15, 20–23]. Various studies in vitro cell experiments [24, 25] show that relative biological effectiveness increases with elevated linear energy transfer, while clinical outcome data are less clear regarding the impact of linear energy transfer on relative biological effectiveness [26–38]. A relative biological effectiveness of >1.1 for adverse events associated with higher linear energy transfer within organs at risk has been reported for rib fracture [39], rectal bleeding [40], mandible osteoradionecrosis [41, 42], brain necrosis [26, 28, 34, 43], and late-phase pulmonary changes [29] in cancer patients treated with proton therapy. An improved understanding of the relationship between physical dose, linear energy transfer, and adverse events in proton therapy planning is greatly needed to improve treatment planning. Several phenomenological and mechanistic relative biological effectiveness models have been developed to calculate relative biological effectiveness from linear energy transfer and physical dose [44–53]. However, systematic evaluations have shown that in vitro relative biological effectiveness predictions can vary greatly across different models [54]. This significant variability is largely due to the use of tissue-specific a/b ratios in these models, which themselves can have significant parameter uncertainties [45, 55]. Moreover, substantial discrepancies have been reported between in vitro and in vivo relative biological effectiveness results [24]. Since outcomes from clonogenic assays do not necessarily reflect the clinical responses of cancer patients undergoing proton therapy, current relative biological effectiveness models are hindered by considerable biological and parametric uncertainties, limiting the clinical application of linear energy transfer. In clinical practice, a fixed relative biological effectiveness value of 1.1 represents a higher cell-killing effect compared to photons. Proton therapy planning typically relies solely on dose calculations and overlooks critical linear energy transfer information as well as variable relative biological effectiveness of tumors based on histology and fraction size [17, 18]. This oversimplification has adversely affected the efficacy of proton therapy, leading to unexpected adverse events that place additional burdens on the healthcare system and increase financial costs [20, 56–58]. Therefore, there is an urgent need to incorporate linear energy transfer considerations into plan optimization and evaluation to reduce adverse events. Therefore, there is an urgent need to investigate the effects of physical phenomena resulting from the interaction of the proton beam with water.
Therefore, in this regard, we analyze the different processes when a proton beam irradiates the water with two methods of Maple programing and GEANT4 simulation [7]. Thus, the article is organized as follows. In section 2, we analyze the interaction of protons with matter. In section 3, we study the inelastic processes that contribute to the total cross-section for protons passing through water phantom, and therefore, we follow the approach and use data in Refs. [3, 6] to calculate cross-sections for different processes such as ionization, excitation, stripping and charge transfer. In section 4, we will shortly become familiar with the GEANT4 toolkit. Also, the fragmentation of particles and processes like straggling, which determine the height and the width of the Bragg's peak are also described in this section. In Section 5, our numerically obtained results are described. Finally, we give a summary of our work.

2-Interaction of proton with matter

2-1-Stopping power

For charged particles other than electrons with charge number z moving in a target material of atomic number Z and density ρ with velocity β, the mean ionization energy loss (or electronic stopping power) can be described by the Bethe-Bloch equation [12-14]:

$$\frac{1}{\rho}\frac{dE}{dx} = Kz^2\frac{Z}{A}\frac{1}{\beta^2}\left[\frac{1}{2}\ln\frac{2m_e c^2\beta^2\gamma^2 T_{max}}{I^2} - \beta^2 - \frac{\delta(\beta\gamma)}{2}\right] \quad (1)$$

with $K = 4\pi N_A r_e^2 m_e c^2$, N_A Avogadro's number, r_e and m_e are the radius and mass of the electron, , I is the mean ionization potential of the material. Furthermore, $\delta(\beta\gamma)$,is the density effect correction to ionization energy loss, β and γ ($\gamma = 1/\sqrt{1-\beta^2}$) are the usual relativistic factors. Here, T_{max} is the maximum of kinetic energy which can be imparted to a free electron in a single collision , which is given by:

$$T_{max} = \frac{2m_e c^2 \beta^2 \gamma^2}{1 + 2\gamma m_e/M + (m_e/M)^2}$$

It is important to note that the deposited energy is inversely proportional to the square of particle velocity. Upon entering the matter, the protons have maximum energy and therefore maximum velocity but as they traverse the matter they interact with the orbiting electrons, lose energy and velocity and deposit more and more dosage. Physically, the dependence on arises from the time needed for a Coulomb interaction to take place. If the particle moves faster, there is less time for the electric fields of the projectile and the atoms in the matter to interact, and thus less energy is deposited. The average energy deposited to the matter by radiation per unit mass of this matter is called the dose deposited by an ion beam : $D = 1.602 \times 10^{-10} \times \varphi \times \frac{dE}{\rho dx}(Gy)$, where, $\frac{dE}{\rho dx}$ in $\frac{\text{MeV.cm}^2}{\text{g}}$ is mass stopping power (see equation 1) and φ is the number of charged particles per cm^2.in this work $\varphi = 10^6 \text{cm}^{-2}$.

2-2-Range straggling

The loss of energy of an ion within matter is a statistical process, and it is not definite, and the Bethe equation yields only the average of energy lost. This change was first described by Bohr, who introduced energy straggling ($\sigma_E(x)$) by the relation: $\frac{d\sigma_E^2(x)}{dx} = K(x) - 2\frac{dS(E(x))}{dx}\sigma_E^2(x)$ where $K(x) = z^2 \rho_e K \frac{1-\frac{1}{2}\beta^2}{1-\beta^2}$ here ρ_e is electron density and other parameters introduced previously .Therefore, range straggling (σ_R) is defined as a function of energy from the solution of the $\frac{d\sigma_R^2}{dx} = \frac{1}{S(E)}\frac{d\sigma_E^2(x)}{dx}$ equation, where , S(E) is the total mass stopping power. Protons which pass through the matter may be deflected by the atomic nucleus. This process is commonly referred to as scattering, or more precisely, a multiple coulomb scattering is observed, when angular scattering occurs due to the collective effect of many small single-scattering which are randomly happened. Both the proton and the nucleus are positively charged. Therefore, their interactions are mostly Columbic.

2-3-Continuous Slowing Down Approximation (CSDA) range:

The range of protons can be calculated by some numerical integration methods. But Continuous Slowing Down Approximation (CSDA) is a simple and common method to calculate the range of the heavy particles like protons in the targets and this method is employed in this study. The CSDA range is the average distance a proton travels before stopping, calculated by integrating the inverse of the stopping power: $CSDA\ R = \int_{E_f}^{E_0} \frac{dE}{S_{tot}}$, here E_0 and E_f are the initial and final energy of the proton input at the target also S_{tot} is stopping power or $\frac{dE}{dx}$. Incident particles continuously lose their energy in the path of the targets and the CSDA method neglects energy loss fluctuations. In this work, we use the CSDA method to calculate the proton range.

2-4-Multiple Coulomb Scattering

Besides inelastic collisions with the atomic electrons, a charged particle also suffers numerous elastic Coulomb scatterings from the nuclei themselves. The energy loss as a result of multiple Coulomb scattering (MCS) is negligible, but it is nevertheless important for dosimetry, because it causes lateral broadening of the pencil beam. Theoretical calculations of the scattering angle are highly complex. One of the most complete derivations was performed by Molière [21], and various calculations in order to derive more practical formulas were performed afterward, for instance by Lewis [22], Highland [23], and Gottschalk [24]. Due to the Central Limit Theorem, the probability distribution of the net angle of deflection of a particle in a thick material is very nearly Gaussian, resulting from the sum of many small random deflections. An approximation for the probability distribution for the net angle of deflection by MCS in a material was derived by Highland [23], and can be approximated by a Gaussian distribution with a width given by: $\theta_0 = \frac{14.1MeV}{pv} z_p \sqrt{\frac{L}{L_R}}\left[1 + \frac{1}{9}\log_{10}\left(\frac{L}{L_R}\right)\right]\text{rad}$, where p is the proton momentum and v = βc is the proton velocity and L is the target thickness and is the target radiation length. The length of the radiation is the distance that the energy of the radiation particles due to radiation losses decreases as much as the coefficient e^{-1} (≈ 0.37).

3-Proton passage through water phantom

3-1-Inelastic cross section

In the beginning, we have studied the passage of a single proton through liquid water. When the energetic ion enters the matter, inelastic cross sections are typically small, but they grow to reach a maximum, namely the Bragg's peak, where the ion loses its energy at the highest rate. For our analysis, we primarily follow the

approach outlined by Ding et al. [3]. First, we consider impact ionization, which is the dominant process contributing to the energy loss and resulting in the production of secondary electrons, and then add several other terms, such as excitation, charge transfer, stripping and ionization by protons. The secondary electrons are not produced by the process of excitation. The charge transfer phenomenon involves the transfer of electrons from water molecules to the projectile, which are ultimately neutralized. When the projectile of a proton is discussed in this study, charge transfer involves the transfer of one single electron. The hydrogen atom formed can also ionize the matter or can become stripped, in which case it loses the previously absorbed electron.

3-2- Ionization by protons

The singly differentiated cross section, SDCS, is the basic quantity in the analysis of the ionization process. This shows the total ionization cross-section differentiated concerning the energy, , of the ejected electrons and is dependent on the kinetic energy of the projectile, T. We use a semi-empirical expression introduced by Rudd and co-workers [6], which was derived by adjusting the experimental data to the Rutherford cross-section, among other analytical models,

$$\frac{d\sigma(W,T)}{dW} = z^2 \sum_i \frac{4\pi {a_0}^2 N_i}{B_i}\left(\frac{R}{B_i}\right)^2 \times \frac{F_1(v_i)+F_2(v_i)\omega_i}{(1+\omega_i)^3\left(1+exp\left(\alpha\left(\omega_i-\omega_i^{max}/v_i\right)\right)\right)} \quad (2)$$

Where the sum is taken over the five electron shells of the water molecule, is the Bohr radius, is the Rydberg constant, is the shell occupancy, is the ionization potential of the sub-shell for water vapor, is the dimensionless normalized kinetic energy of the ejected electron. The dimensionless normalized velocity,, is given by [5]

$$v_i = \sqrt{\frac{mV^2}{2B_i}} \quad (3)$$

where, is the mass of the electron and is the velocity of the projectile, which in the relativistic case is given by βC , also,

$$\beta = \sqrt{1-\frac{1}{\gamma^2}} = \sqrt{1-\left(\frac{Mc^2}{Mc^2+T}\right)^2} \quad (4)$$

where, is the mass of the projectile. Eq. (3) uses the kinetic energy of an electron having the same velocity as the projectile, normalized by the corresponding binding energy. The expressions for the functions in Eq. (2) are

$$F_1(v) = A_1 \frac{ln(1+v^2)}{B_1/v^2+v^2} + \frac{C_1 v^{D_1}}{1+E_1 v^{D_1+4}} \quad (5)$$

$$F_2(v) = C_2 v^{D_2} \frac{A_2 v^2 + B_2}{C_2 v^{D_2+4} + A_2 v^2 + B_2} \quad (6)$$

$$W_i^{max} = 4{v_i}^2 - 2v_i - \frac{R}{4B_i} \quad (7)$$

Eqs. (5)– (7) show original non-relativistic expressions for the Rudd model. is calculated classically as a function of . The parameter set for the protons SDCS used in this work can be found in Table 1 and were calculated by Dingfelder and co-workers [3]. Surdutovich et al. [5] introduce some modifications to which account for the relativistic effects due to the high energies reached (up to β~0.6),

$$F_1^{rel}(v) = A_1 \frac{ln\left(1+v^2/1-\beta^2\right)}{B_1/v^2+v^2} + \frac{C_1 v^{D_1}}{1+E_1 v^{D_1+4}} \quad (8)$$

Table 1. Required parameters for the SDCS of protons on water (from Refs. [3,6]).

parameter	Outer shells		Inner shells
	Liquid	Vapor	K-shells
A_1	1.02	0.97	1.25
B_1	82.0	82.0	0.50
C_1	0.45	0.40	1.00
D_1	-0.80	-0.30	1.00
E_1	0.38	0.38	3.00
A_2	1.07	1.04	1.10
B_2	14.6	17.3	1.30
C_2	0.60	0.76	1.00
D_2	0.04	0.04	0.00
α	0.64	0.64	0.66

When we expand the Rudd's model to relativistic energies, we note that F_1 and F_2 tend to $A_1 \ln(v^2)/v^2$ and A_2/v^2, respectively. Since F_2 approaches zero faster, F_1 absorbs the relativistic corrections. This results from the fact that as $A_1 \sim A_2$, for high velocity $(v \gg 1)$, F_1, is always higher than F_2. In particular, the new F_1^{rel} introduced by Surdutovich and co-workers [5] reproduces the same asymptotic behavior as the Bethe-Bloch formula. In this work, the Rudd model with relativistic corrections has been employed to account for the ionization process. The parameter set for the SDCS of protons on water vapor is also given in 1992 by Rudd et al. [6] and are also shown in Table 1. The division into inner and outer shells that Rudd suggests for choosing one or another set of parameters has been accepted. However, we followed the approach from Ref. [3], which consists of separating the K-shell from the rest, as seen on Table 3. In their investigation, Rudd and co-workers reviewed the different approaches for the total cross sections and suggested this semi-empirical approach. According to Ref. [3], the latter does not reproduce accurately the stopping cross section for liquid water due to the lack of careful consideration of the water molecule's subshells. To overcome this, they suggest adding a partitioning factor G_j which adjusts the contributions of the sub-shells to the results from the Born approximation.

$$\frac{d\sigma}{dW} = \sum_{all\ j} G_j \frac{d\sigma^j}{dW_j} \qquad (9)$$

In this work, we reproduce the previous expressions for liquid water from Ding elder et al. [3] directly, who obtained the parameter set for liquid water by modifying the water vapor set until the equations reproduced the recommended ICRU stopping cross section for the desired material [8].

It must be noted that Rudd and co-workers developed their model for vapor water, and took the binding energies for this phase as parameters. Hence, even though our approach is for liquid water, the binding energies used in the SDCS (Eqs. (2), (3) and (7)) are those from water vapor. By integrating the SDCS over the secondary electron energy,, the total cross section of impact ionization by the ion with kinetic energy is obtained:

$$\sigma(T) = \int_0^{W_{max}} \frac{d\sigma(W,T)}{dW} dW \qquad (10)$$

The maximum kinetic energy is

$$W_{max,i} = T - I_i \qquad (11)$$

Note that in this case, the binding energy corresponds to that of liquid water.

Table 2. Ionization energies (in eV) for the different sub-shells in the water vapor () and liquid water (), the partitioning function and the number of electrons . The data are taken from Ref. [3].

Shell	Outer shells				Inner shells
	$2a_1$	$1b_2$	$3a_1$	$1b_1$	$1a_1$
I_j	32.30	16.05	13.39	10.79	539.00
B_j	32.20	18.55	14.73	12.61	539.70
G_j	0.52	1.11	1.11	0.99	1.00
N_j	2	2	2	2	2

Table 3. required parameters for the excitation cross section for liquid water, taken from [3].

k	Excited state	E_k (eV)	a (eV)	J (eV)	Ω	v
1	A~^1 B_1	8.17	876	19820	0.85	1
2	B~^1 A_1	10.13	2084	23490	0.88	1
3	Ryd A+B	11.31	1373	27770	0.88	1
4	Ryd C+D	12.91	692	30830	0.78	1
5	Diffuse bands	14.50	900	33080	0.78	1

3-3- Excitation by protons

For the case of excitation of the molecules of liquid water, we use a semi-empirical model which relates proton excitation cross section to electron excitation cross section, developed by Miller and Green [9]. The cross section for a single excitation of an electron in sub-shell is given by the expression:

$$\sigma_{exc,k}(T) = \frac{\sigma_0 (Za)^{\Omega} (T - E_k)^{v}}{J^{\Omega+v} + T^{\Omega+v}} \qquad (12)$$

where , is the number of electrons in the target material and is the excitation energy for the state . ‘ ‘and are parameters (shown in Table 3), but they have physical meaning: and (dimensionless) represent the high energy limit , and (dimensionless) the low energy limit. We have taken the values recommended by Ding elder and his group, who in turn used the original suggestions in Ref. [9].

3-4- Charge transfer

There exists the possibility that an electron from the water joins the projectile, the proton in this case. A neutral hydrogen atom is then formed either in a bound state or in a state in which the electron travels with the proton at the same velocity. This phenomenon is known as charge transfer. Again, following Ding elder's approach [3], who showed the contribution of the charge-transfer cross section by an analytical formula:

$$\sigma_{10}(T) = 10^{Y(X)} \qquad (13)$$

Where with T measured in eV and

$$Y(X) = [a_0 X + b_0 - c_0 (X - x_0)^{d_0} \Theta(X - x_0)]\Theta(x_1 - X) + (a_1 X + b_1)\Theta(X - x_1)$$

Where $\Theta(X)$ is the Heaviside step function and the other parameters is can be found in Table 4.
oss section, taken from [3].
These parameters were obtained by considering the experimental data on water vapor [10–12] as a starting point and adjusting them to fit the contribution of the charge transfer to the total cross section in the recommended values for liquid water. The subscripts 1 and 0, in the charge transfer cross section mean that the projectile goes from state 1 to state 0, where 1 corresponds to a proton and 0 to a neutral hydrogen.

3-5- Stripping of neutral hydrogen

The neutral hydrogen atom can undergo stripping or electron loss. As before, not much experimental data exists for liquid water. Hence, we decided to use a semi-empirical formula given by Rudd et al. [13] for the cross-section. In this expression, the harmonic mean of a low energy and a high energy part is considered. Parameters used are those obtained by Ding elder and his group to fit the recommended values for liquid water.

$$\sigma_{01}(T) = \left(\frac{1}{\sigma_{low}} + \frac{1}{\sigma_{high}}\right)^{-1} \qquad (15)$$

The two parts of the stopping cross-section may be calculated as

$$\sigma_{low}(T) = 4\pi {a_0}^2 C \left(\frac{\tau}{R}\right)^{D} \qquad (16)$$

$$\sigma_{high}(T) = 4\pi {a_0}^2 \left(\frac{R}{\tau}\right)\left[A \ln\left(1 + \frac{\tau}{R}\right) + B\right] \qquad (17)$$

Where A, B, C and D are fitted parameters as given in Table 5. R=13.6eV is the Rydberg constant and is the kinetic energy of an electron traveling at the same speed as the proton.

3-6- Ionization by neutral hydrogen

The last effect to be taken into account is the ionization by neutral hydrogen. Despite the lack of direct experimental information on this process, Bolorizadeh and Rudd [14] concluded that the ratio of the SDCS for hydrogen impact to the SDCS for proton impact as a function of the energy of the secondary electron is independent of this parameter when the projectile energy is fixed. We can use the SDCS for protons as the starting point and correct it by a factor $g(T)$ that depends only on the particle energy $T(eV)$, that is:

Table 3. required parameters for the charge transfer cross section, taken from [3].

a_0	b_0	c_0	d_0	a_1	b_1	x_0	x_1
-0.180	-18.22	0.215	3.550	-3.600	-1.997	-3.450	5.251

Table 4. required parameters for the stripping total cross section, taken from [3].

A	B	C	D
2.835	0.310	2.100	0.760

$$\left(\frac{d\sigma}{dE}\right)_{hydrogen} = g(T)\left(\frac{d\sigma}{dE}\right)_{proton} \quad (18)$$

Where the correcting function is adjusted by Ding elder and his group to fit the values for liquid water provided by ICRU 49 [8].

$$g(T) = 0.8(1 + exp\left[\frac{\log(T) - 4.2}{0.5}\right])^{-1} + 0.9 \quad (19)$$

3-7-From the total cross section to the LET

The total cross sections for the different processes considered above for protons in liquid water with charge transfer cross section is higher for low energies of the projectile, but it falls to zero very fast for energies around 0.1MeV. It is then expected that only for low energies, the probability of finding the projectile as a neutral hydrogen becomes important.

3-8- Probabilities of charge state and stopping cross section

The combination of the contributions to the total stopping cross-section has to be done in such a way that it takes into account the state of the projectile. In the case of a proton, we have just considered two possible charge states: neutral hydrogen $(H, i = 0)$ and proton $(P, i = 1)$. The total stopping cross section will be the sum of all charged states of the particle [3],

$$\sigma_{st} = \sum_{i,j,i\neq j} \Phi_i\left(\sigma_{st,i} + \sigma_{ij}T_{ij}\right) \quad (20)$$

Where the term T_{ij} denotes the energy loss in the charge changing process, from state to state . Only one electron will be ripped out from the water molecule in the charge transfer process, and so we can suppose the most probable sub-shell to undergo the reaction is that with the smallest binding energy. This way we can establish a lower bound for the sum $T_{01} + T_{10}$ as the ionization energy of water plus the kinetic energy of the electron,

$$T_{01} + T_{10} = I_0 + \frac{mv^2}{2} \quad (21)$$

and Φ_i is the probability that the projectile is in state. This is determined by the charge transfer and the stripping cross-section:

$$\Phi_0 = \frac{\sigma_{10}}{\sigma_{01} + \sigma_{10}} \quad (22)$$

$$\Phi_1 = \frac{\sigma_{01}}{\sigma_{01} + \sigma_{10}} \quad (23)$$

Eq. (20) may now be rewritten as

$$\sigma_{st} = \Phi_0\sigma_{st,0} + \Phi_1\sigma_{st,1} + \sigma_{st,CC} \quad (24)$$

$$\sigma_{st,CC} = \frac{\sigma_{01}\sigma_{10}}{\sigma_{01} + \sigma_{10}}(I_0 + \tau) \quad (25)$$

The stopping cross-sections are calculated as

$$\sigma_{st,i} = \int_0^{E_{max}} E\frac{d\sigma_i(E,T)}{dE}dE \quad (26)$$

Where is the maximum energy loss by the projectile in the corresponding inelastic process. The total stopping cross section is compared with the PSTAR values [15]. The reference database for stopping power and range tables for protons (PSTAR) is provided by the National Institute of Standards and Technology (NIST) of the US Department of Commerce. These values are obtained, for high energies, through Bethe's stopping formula including shell corrections, Barks and Bloch corrections [16, 17] and density effect corrections. The mean excitation energy, I, used in PSTAR is taken from ICRU 37 [18], corresponding to $I = 75eV$ for liquid water. For low energies, experimental data in PSTAR are fitted to empirical formulas. By definition, the linear energy transfer is proportional to the stopping cross section

$$\frac{dT}{dx} = -n\sigma_{st}(T) \quad (27)$$

where is the number density of water molecules. The position of the projectile as a function of its kinetic energy is obtained by integrating the inverse of LET [4, 5]

$$x(T) = \int_T^{T_0} \frac{d\acute{T}}{|d\acute{T}/d\acute{x}|} \quad (28)$$

where T_0 is the initial energy of the projectile. The parametric representation of LET versus depth is known as the depth-dose distribution. This process, used to calculate the energy transfer, is known as the Continuous Slowing Down Approximation (CSDA). In this approximation, the projectile is assumed to lose energy in a continuous way. However, energy loss by a proton is a stochastic process, which produces variations in the range of the particles. In addition, the projectile might react with a water molecule and become fragmented. Then, for a real model, we need to include two important contributions: straggling and nuclear fragmentation.

3-9- Straggling and fragmentation

Straggling accounts for the stochastic fluctuations in the range of the particles that traverse the medium. The straggling model considered here goals that the ranges

of the projectiles follow a Gaussian distribution. The so-called broad-beam depth-dose curve results from the convolution of the previously CSDA LET with this Gaussian range straggling distribution. The concept is known as "depth scaling" and was introduced by Carlson et al. [19]. For each point x in the trajectory, it is assumed that every particle in the beam has an effective penetration depth $\acute{x}$. These effective depths are distributed as a Gaussian centered on the actual penetrated depth x, which coincides with the CSDA range.

$$\pi(x,\acute{x}) = \frac{1}{\sqrt{2\pi}\sigma_{strag}(x)} \exp\left(-\frac{(\acute{x}-x)^2}{2{\sigma_{strag}}^2(x)}\right) \quad (29)$$

Where σ_{strag} is the variance, which may be obtained from a phenomenological formula given by Chu et al. [20] and depends in general on . Nevertheless, the shape of the depth-dose distribution allows us to assume that it is approximately constant, with $\sigma(x) \sim \sigma(R_0)$ [21], since most of the curve is approximately flat and will not be significantly affected by the convolution. The expression for $\sigma_{strag}(x)$ is given by:

$$\sigma_{strag}(x) = 0.012x^{0.951}A^{-0.5} \quad (30)$$

Where A denotes the ion's mass number [21]. Straggling has two important consequences on the depth-dose distribution. Firstly, as fewer particles arrive at the same final position, the dose at the peak is considerably reduced.

In addition, different particles have different ranges, and thus the peak is broadened. Nuclear fragmentation accounts for the possibility that when the projectile hits a target, it undergoes fragmentation. Two different effects need to be considered. The first one is the reduction of the beam fluence, lowering the height of the depth-dose distribution at the peak. On the other hand, fragments can be produced in the same direction as the original beam. If lighter elements are formed, as having a longer range, they produce a tail in the depth-dose distribution which goes clearly beyond the position of the Bragg peak maxima. For protons, fragments are not important and so a tail is not observed. Hence, in this work we only include fragmentation by considering the reduction in the number of particles of the beam. This model deals with a pencil beam with a single projectile, so the concept of fluence loses its meaning within this context (it would be a Dirac delta function). Instead, the fragmentation effect is considered through the decay of the total number of particles. If the projectile has the probability of P reacting with a water nucleus, then:

$$\frac{dN(x)}{dx} = -PN(x) \quad (31)$$

$$N(x) = N_0 e^{-Px} = N_0 e^{-x/\lambda} \quad (32)$$

where λ is called the mean free path length and N_0 is the initial number of incident protons. From the prediction of Ref. [22], we have $\lambda = 435\ mm$, for protons in liquid water. The broad-beam depth-dose curve, considering fragmentation and straggling, is therefore calculated as

$$\langle\frac{dT}{dx}(x)\rangle = N(x)\int_0^{R_0} \pi(x,\acute{x})\frac{dT}{d\acute{x}}d\acute{x} \quad (33)$$

There is one additional process which has not been considered, multiple scattering, which accounts for the divergence of the beam as it travels through the matter. It has been shown that multiple scattering produces changes in the shape of the Bragg peak [23], especially in the amplitude and the peak to entrance dose ratio, although not in the range. Usually, hadron therapy simulations merely apply normalization procedures to fit the experimental data [24], as the effect is only due to a reduction of the fraction of primary particles. To compare with experimental data, the current model normalizes the depth-dose distribution to the experimental entrance dose, and so scattering is not included.

4-GEANT4 Simulation

The GEANT4 code version 10.1.1 was used for this research. The physics lists adopted in this research were based on the suggestions from the user guide and recommended settings in other works [10, 11]. GEANT is a toolkit for the simulation of radiation transport in materials. It suggests a set of physics models based on theoretical and experimental data. GEANT works based on a C++ program. The experimental setup has to be explicitly described in the code, the primary particles have to be provided, and the specific physics models to be used in the simulation should be included in the code. GEANT also represents some extra visualization tools. (for example, OpenGL, Wired, Ray Tracer, etc.). The materials and geometry part of the main part is used to interpret the detector. The user has to form a concrete class from the G4VUserDetectorConstruction abstract based on class. In the implicit method, all the required materials, the detector geometry volume, and the classes of sensitive detec-

tors have to be made.
The classes of sensitive detectors should be set to the volumes of detectors. The physics part of the code is where the physics processes are selected and the particle interactions with matter are defined. GEANT4 does not have any default particles or processes; it has to be explicitly defined within the code. A concrete class can be derived from the G4VUserPhysicsList abstract class. This concrete class should define all the required particles, all the required processes which should, in turn, be assigned to proper particles, and the cut-off ranges applied to the world. A step in GEANT4 has two points and carries information such as the energy loss on the step and time-of-flight spent by the step of a particle. In case a step is limited by a volume boundary, the endpoint physically stands on the boundary and it logically belongs to the next volume. Since each step knows two volumes, boundary processes such as reflection and radiation of transition can be simulated. GEANT4 tracking is general; it is independent of the particle type and the physics process related to a particle. While a process is being tracked in GEANT4, it contributes to any possible changes in the physical quantities of the track. Each process can also create secondary particles and suggest variations in the state of the track. At the start of a process, an event contains primary particles. To create the primary event, the concrete class has to be derived from the G4VUserPrimaryGeneratorAction abstract base class. A G4Event object is passed to one or more primary generator concrete class objects, which generate primary vertices and primary particles. These primaries are pushed into a stack. When the stack is empty, the processing of an event is over. A G4Event class shows an event. Each event generates a primary vertex and particle list, hits collections, path collection, etc. This information is then sent to the run manager. A run is a collection of events that share the same detector conditions. A run in GEANT4 begins with the command 'Beam On'. Within a run, the user cannot change the geometry of the detector or the settings of the physics phenomena. At the start of a run, the geometry is optimized for orientation, and cross-section tables are estimated in accordance with the materials given in the geometry. For visualization, the user has to derive a concrete class from G4VVisManager following the computer environment. GEANT4 creates interfaces such as RayTracer, WIRED, OPACS, OpenGL, DAWN, and VRML for graphics drivers.
In Hadrontherapy, we suggest the use of the QGSP_BIC_EMY Reference Physics List that has been required and tested by some of the authors of the present paper. It has been specifically created to address simulation problems for which a high level of accuracy is requested. QGSP_BIC_EMY is an acronym that briefly explain all the physics models activated when it is called: QGSP (Quark Gluon String Precompound) defines the hadronic models for nucleons; BIC (Binary Ion Cascade) defines the inelastic models for ions and EMY (Electro-Magnetic Y) defines the electromagnetic models used by all the particles (Y indicates a particular EM physics particularly tailored for the use in medical physics. All the results presented in this paper and which are relative to the simulation of the proton beams, have been obtained using the QGSP_BIC_EMY. The /run/beamOn command in your Geant4 macro file sets the number of events to be simulated. For example, /run/beamOn 100 would simulate 100 events. Each event represents a single simulation instance, and within each event, particles can interact and generate secondary particles, resulting in multiple steps. In this work, 1000000 events are investigated. Also, we selected the proton beam energy range 20 to 250 MeV. This range is chosen because it encompasses the energies needed to reach the maximum depth of tumors encountered in clinical practice. The simulations utilize Geant4's capabilities to model proton interactions with matter, including electromagnetic and hadronic interactions, to accurately predict dose deposition and optimize treatment planning. In this study, the proton pencil beam orientation is considered. The beam was fired from the lateral side of the phantom. The beam was set with a radius sigma of 4 mm.

5-Results and discussion

Today, in the field of medical equipment, various devices emit radiation at their output. Radiation medicine devices are used for two diagnostic or therapeutic purposes. Since the investigation of the effect of energy-carrying radiation on body tissue is being investigated and studied in different ways, therefore, the science of dosimetry, which is a branch of medical physics, has been formed and is always expanding to include the types of energy-carrying beams. Radiation dosimetry has made great progress in the last decade, which is mainly due to the widespread use of radiation therapy. Therefore, the need for a human tissue-simulating system is inevitable. The use of water phantoms in linear accelerators for medical applications is one of

the basic requirements in the calibration and dosimetry of this equipment. Today, the use of a water phantom is one of the most widely used methods for radiation dosimetry. Therefore, in this work, we use a water phantom.

GEANT4 provides data on the depth-dose distribution of protons in a water phantom. One of the capabilities of the GEANT4 code is freedom of action in defining the physics and geometry of the problem, and It is possible to define very complex geometries, and the user can use a wide range of physical processes depending on their needs. This code provides some physical models of high-speed interaction. The spectrum of the particle source can be defined in a text file, and it can be used for this code can be defined in the application of all kinds of electric, magnetic, and even gravity fields, and fields with a complex design can be defined.

In Figs. .1a and b, the three and two-dimensional variations of deposited absorbed dose in terms of proton energy and penetration depth in water phantom by applying Eq.1 using Maple programming and GEANT4 simulation are shown, respectively. By comparing Figs 1a and b, we find that the theoretical and GEANT4 simulation methods are consistent with each other numerically. Also in Fig.1, it is seen that the height and width of Bragg's peaks with increasing proton energy and depth penetration are changed, and with increasing proton energy, the height of Bragg's peak is decreased. As we have already mentioned, highly energetic protons have a lower probability of interacting with matter and, hence, the energy per unit length they deposit is also lower. When their energy decreases, the linear energy transfer increases considerably. They lose their whole remaining energy in a short distance. In this way, the final range of the projectile is mostly determined by the distance traveled before reaching the threshold. In the Bethe-Bloch equation, ionization and arousal are shown by the projectile, and these cases only play a role in the energy of more than 1MeV.

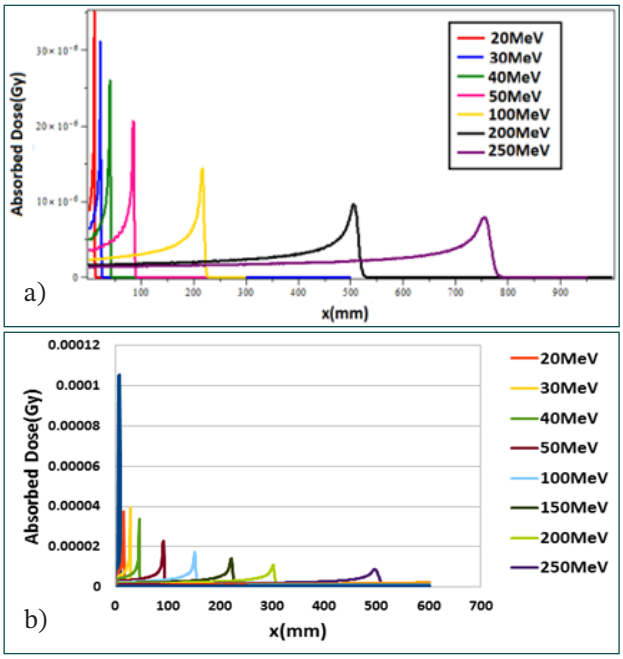

Figure 1: Variations of determined absorbed dose by (a) MAPLE programming and b) GEANT4 toolkit in terms of depth penetration for different proton energies in a water phantom

Figures 1a and 1b are consistent, but because in Figure 1b the Bethe-Bloch stopping power theory is used, taking into account the relative corrections by Barak and Leonard-Stevenson and the shell correction, the height of the peaks is not from high to low, and exceptions are seen due to these corrections. Also, the calculated absorbed dose of the proton beam in this water phantom in this work is in good agreement with Ref [25].

Also, to better understand the consistency of the results obtained from the absorbed dose calculation methods through Maple software and the GEANT4 toolkit, see Table 5.

Table 5. Comparison of absorbed dose results in water phantom in the range of proton radiation energies 20 to 250MeV through Maple software and GEANT4 toolkit in this work

Proton energy (MeV)	20	30	40	50	100	200	250
Absorbed Dose (Gsuperscript with Maple	36	32	26	21	14	9	6
Abrbed Dose (Gy) ×10^(-6) with GEANT4	38	38.5	35	22	18	10	8
Percentage of agreement (%)	5	16	25	4	22	10	25

In Figs 2a, b and c, variations of CSDA R, straggling range, and mean scattering angle of protons in water phantom using GEANT4 simulation as a function of proton energy are shown, respectively.

In Fig.3a, the behavior of dimensionless normalized velocity () versus the ionization potential of the sub-shell () and the kinetic energy of the projectile () for water vapor is plotted. To better understand Fig. 3a, we plotted Figs 3b and c, and Fig. 4. From Fig. 3b, we find that with increasing both and dimensionless normalized velocity () increases. But in Figs.4, we see that is zero at T = 0, but in, with increasing the parameter decreases, nonlinearly.

Fig.5 shows that the the parameter is a function of T, and with increasing T, this parameter increases nonlinearly.

Then, in Fig.6 we plotted the functions of and versus in three different modes according to Table 1._From it we find that with increasing (for liquid and vapor water), both states of outer shells nonlinearly decreases but the inner shell state increases, while has the opposite behavior.

In Fig. 7, it is seen that is linearly increased with increasing kinetic energyfor five states, which is expressed according to Table 1. Fig. 8 shows the variations of versus for three different modes using Table 1. According to this Fig., the outer shell for both liquid and vapor water decreases with increasing v but for inner shell, this result is inverted.

Afterward, in Fig.9, we investigated the variations of cross section for a single excitation of an electron versus kinetic energy for the different sub-shells.It is seen that for with increasing kinetic energy , the cross-section for a single excitation of an electron is equal to zero and for up to is equal to zero and then extends nonlinearly from 45 onwards. But for , at first it decreases and then increases.

Then in Fig. 10, the charge transfer cross-section from 0 to one and two parts of the stopping cross-section with increasing kinetic energy increase, but charge transfer cross-section from 1 to 0 decreases nonlinearly.

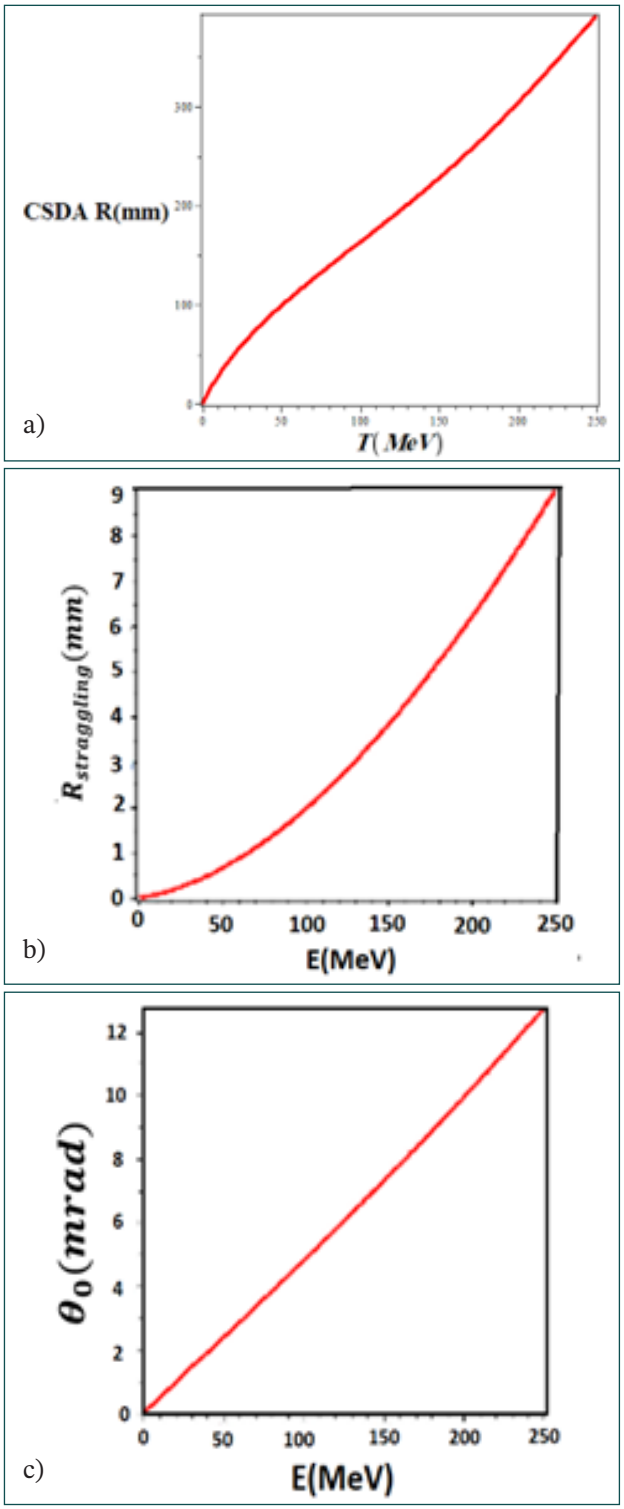

Figure 2: Variations of determined absorbed dose by (a) MAPLE programming and b) GEANT4 toolkit in terms of depth penetration for different proton energies in a water phantom

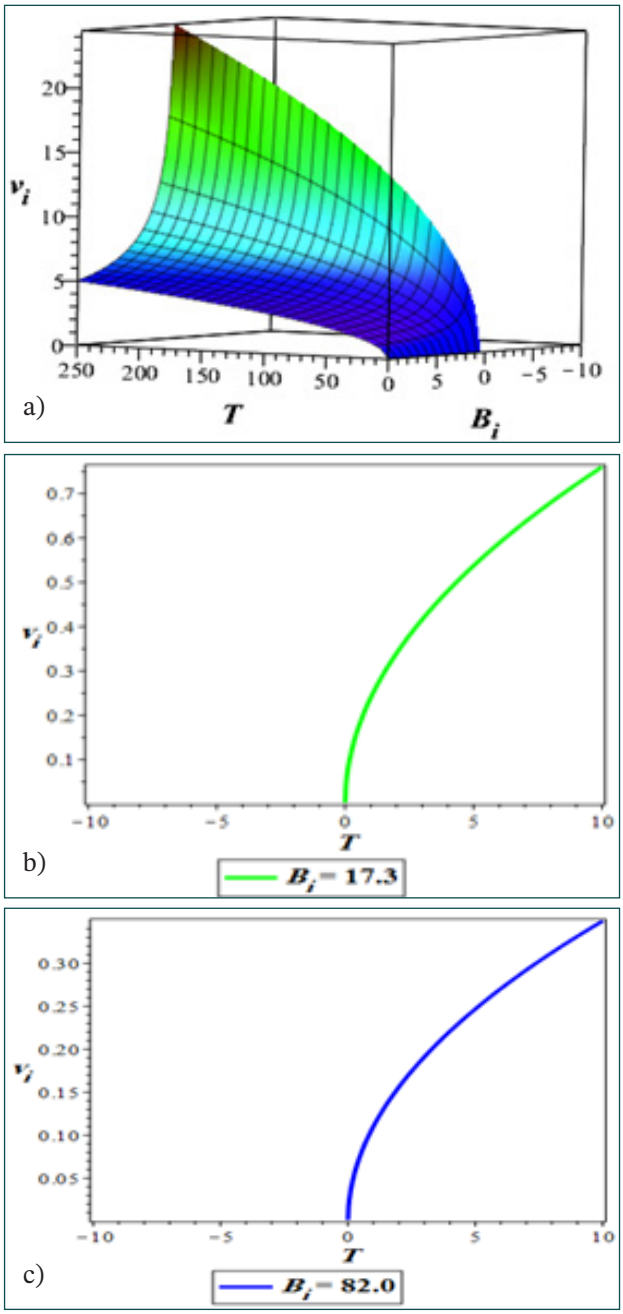

Figure 3: a)Three b)two c)two dimensional variations of dimensionless normalized velocity (v_i) versus the ionization potential of the sub-shell i (B_i) and the kinetic energy of the projectile (T) for water vapor.

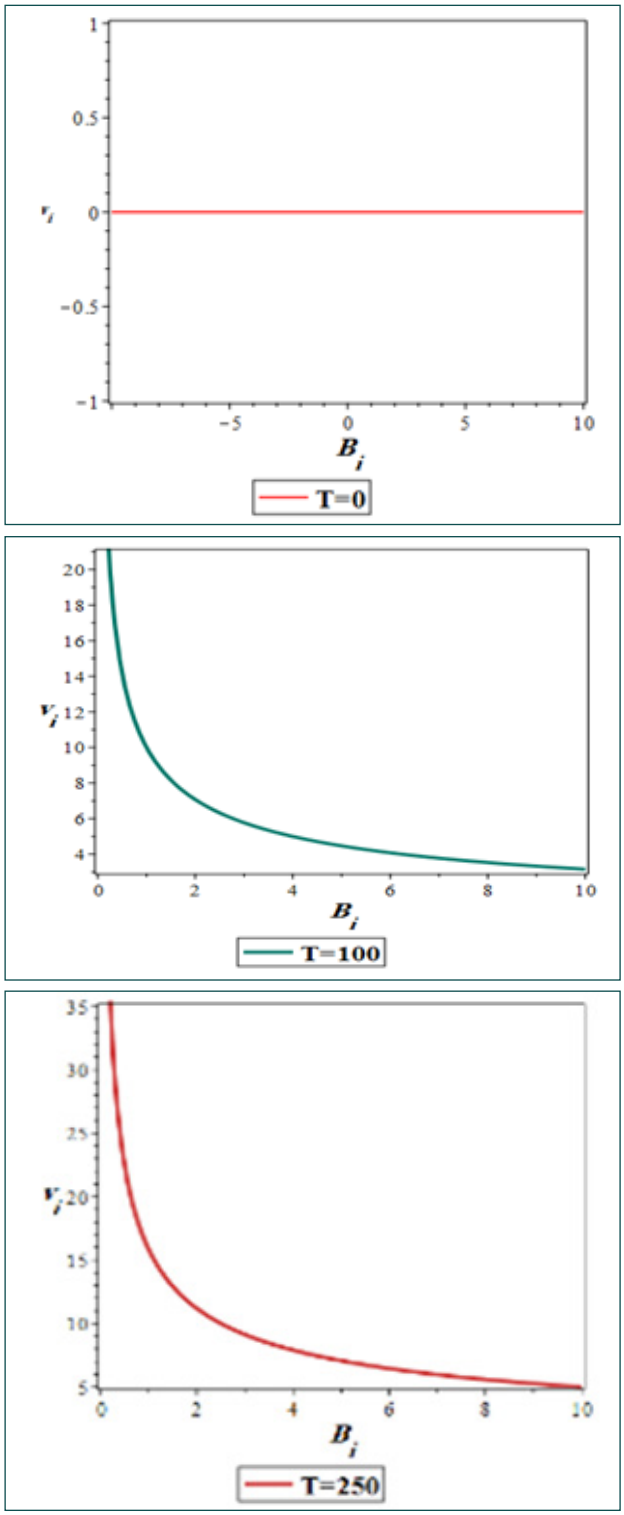

Figure 4: Variations of dimensionless normalized velocity (v_i) versus the ionization potential of the sub-shell i for water vapor (B_i) in different kinetic energy of the projectile (Tin MeV)

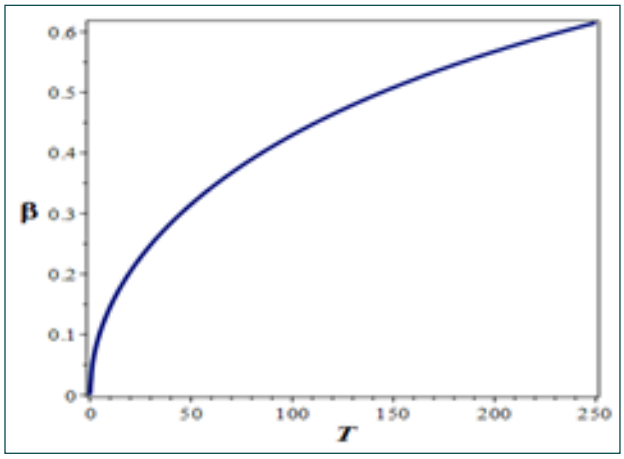

Figure 5: Variations of β versus the kinetic energy of the projectile (T in MeV)

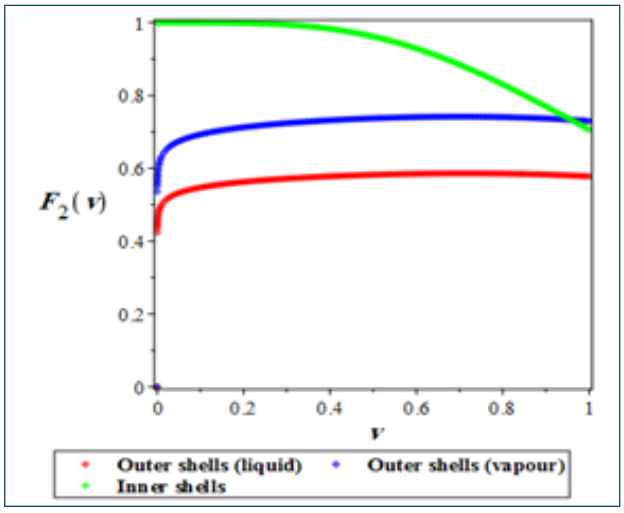

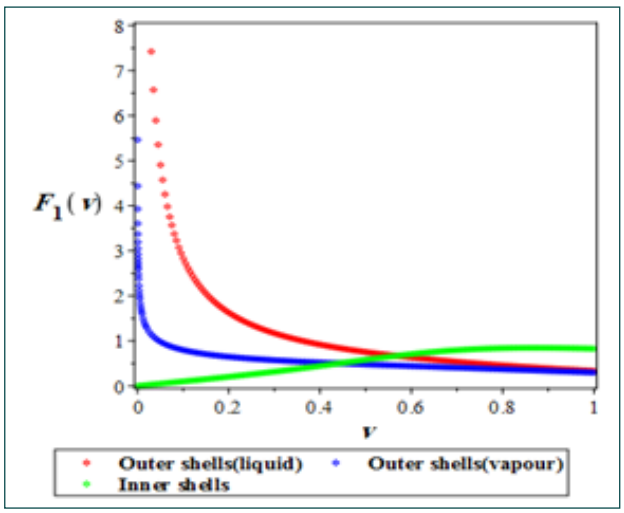

Figure 6: Variations of F_1 (v) and F_2 (v) versus v for different three modes using Table 1.

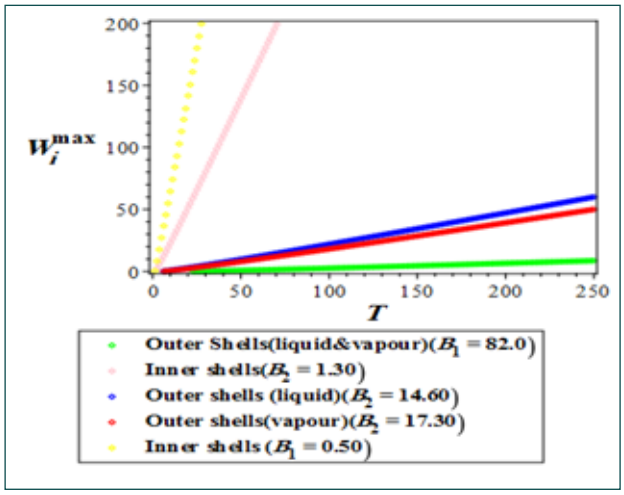

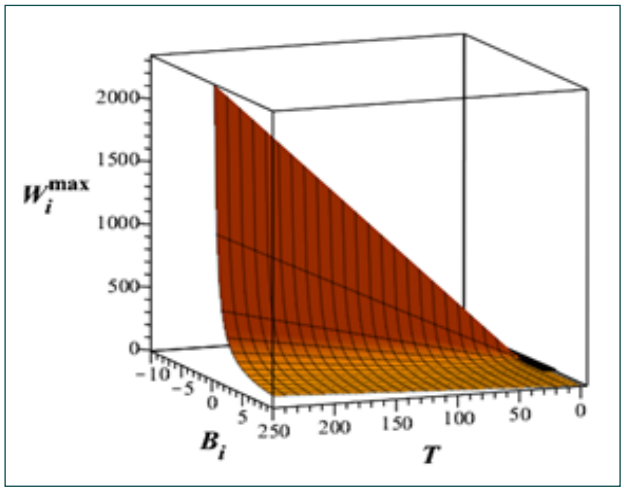

Figure 7: Two and three-dimensional variations of ⟦W_i⟧^maxversus the kinetic energy of the projectile (T) for five different modes of ionization potential of the sub-shell i for water vapor (B_i) using Table 1.

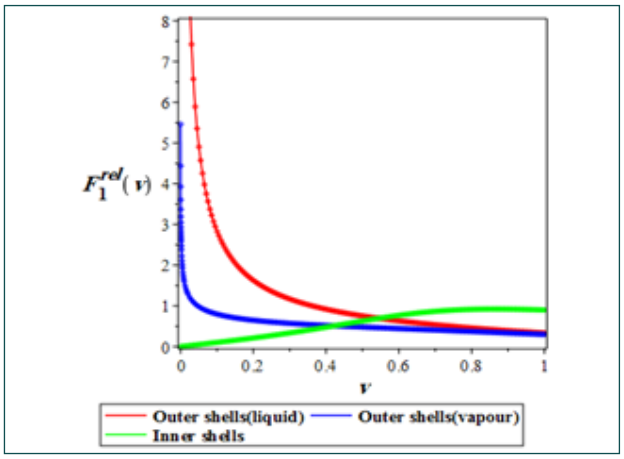

Figure 8: Variations of ⟦F_1⟧^rel (v) versus v for different three modes using Table 1.

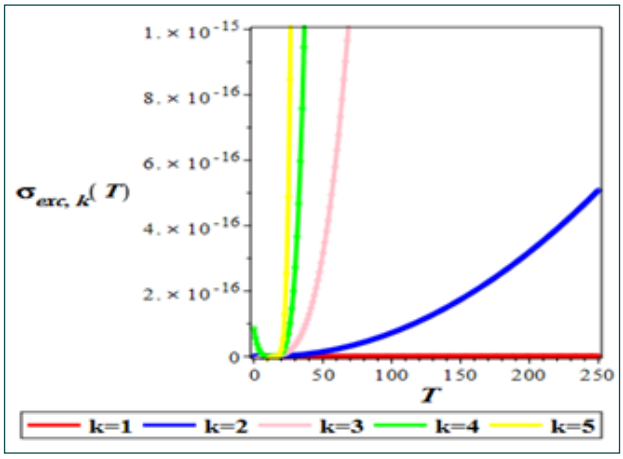

Figure 9: Variations of cross section for a single excitation of an electron (σ_(exc,k) (T)in barn) versus kinetic energy (T in MeV) for the different sub-shell k.

In Fig. 11, we investigated the probability of an object being placed in two positions, one and zero, of the cross-section and the stopping cross-section in both states versus kinetic energy. is fixed in 1, but , and with increasing kinetic energy decreases.

In Fig. 12, the variations of linear energy transfer versus proton energy are shown, which increase nonlinearly with increasing T.

In the end, in Fig. 13, we plotted the 2 and 3 dimensional variations of effective depths versus the actually penetrated depthand effective penetrated depth , we found that in each selected effective depth has one peak.

Bortfeld [26] shows that the relation between the range,, and the initial kinetic energy of the projectile,, is given by:

Where, and is approximately 1.77 for the energy range of 70–250MeV. Fig. 14 shows the range of protons in liquid water for different initial kinetic energies using Eq. (34).

In Fig.14, we see that the) variations as a function of T (in MeV) in water. If we compare this range with the obtained range from GEANT4 simulation (Fig.2a) and also with the calculated range using the semi-empirical model and the Bethe-Bloch formula in Ref. [26], we find that these values are in approximately agreement with the energy range of 70–250MeV, but the estimated range from GEANT4 simulation in this work is more

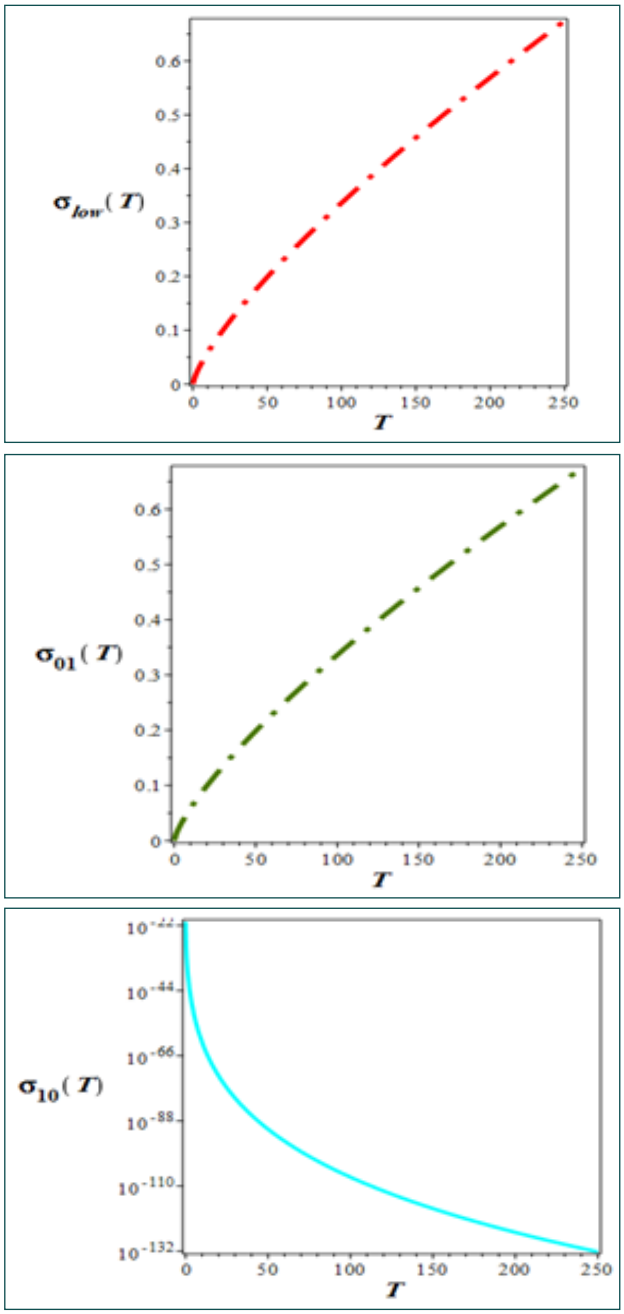

Figure 10: Variations of charge transfer cross section from 1 to zero and from zero to one and two parts of the stopping cross section versus of kinetic energy using tables 4 and 5.

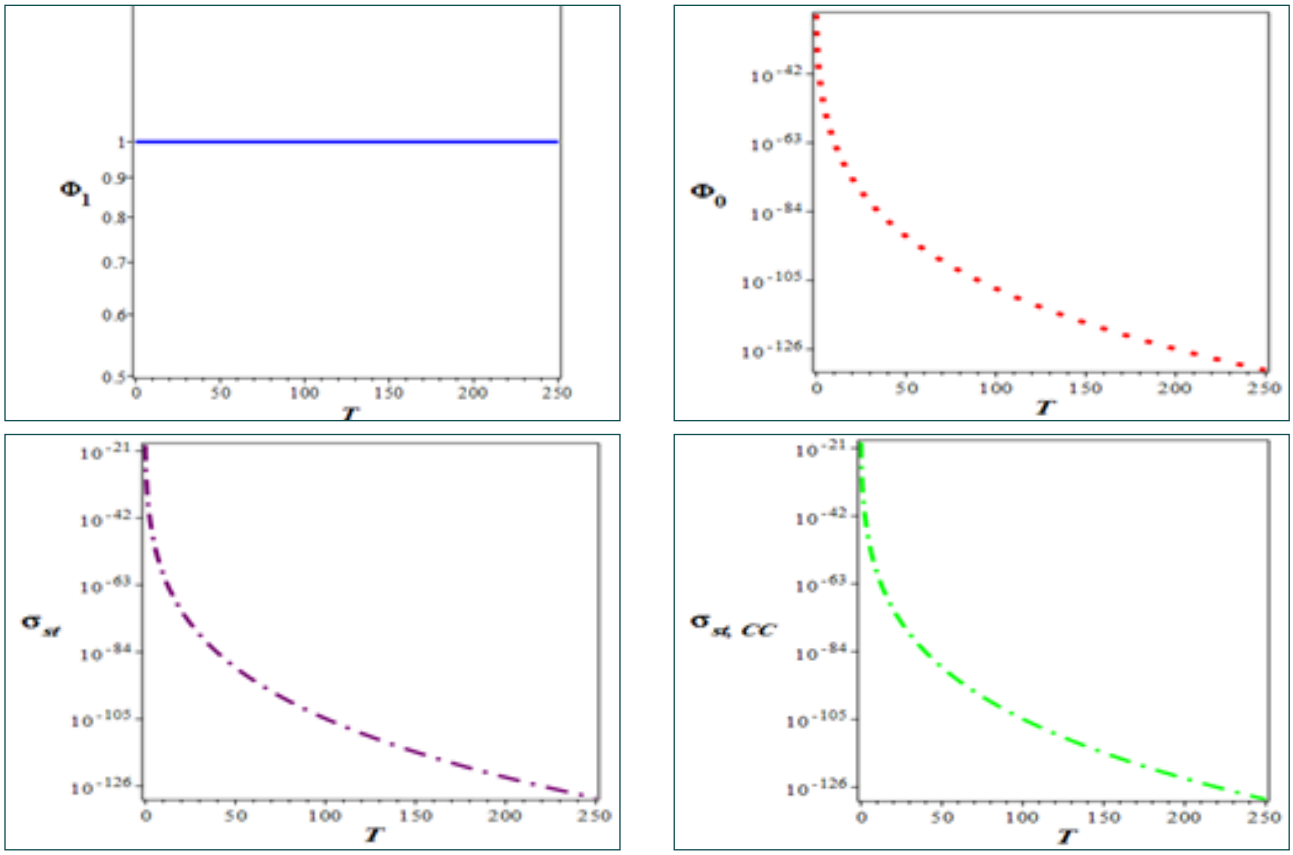

Figure 11: The probability of an object being placed in two positions, one and zero, of the cross section and the stopping cross section in both states versus kinetic energy.

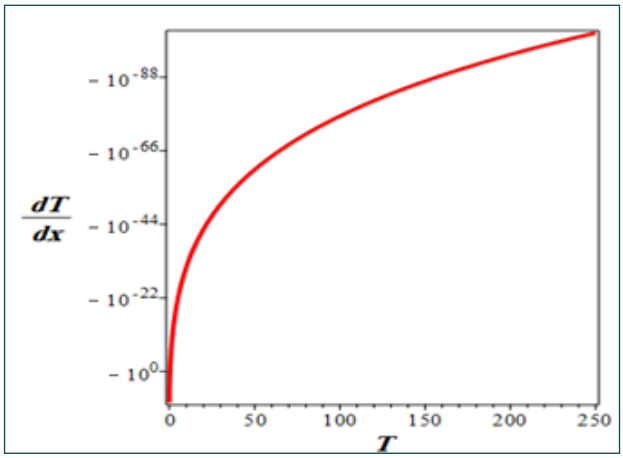

Figure 12: Variations of linear energy transfer proportional to the stopping cross section versus kinetic energy

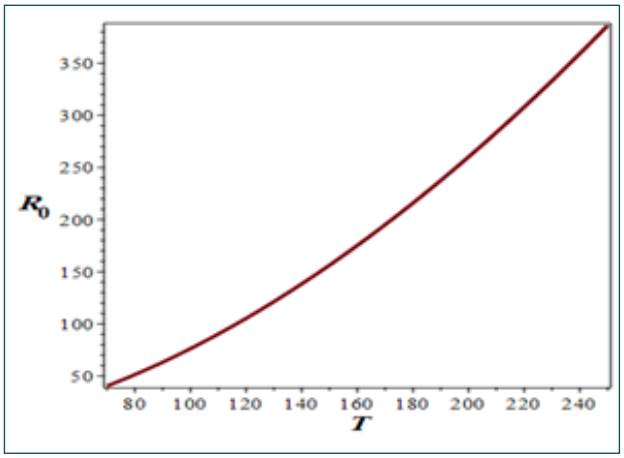

Figure 14: R_0 (in mm) variations as a function of T (in MeV) in water

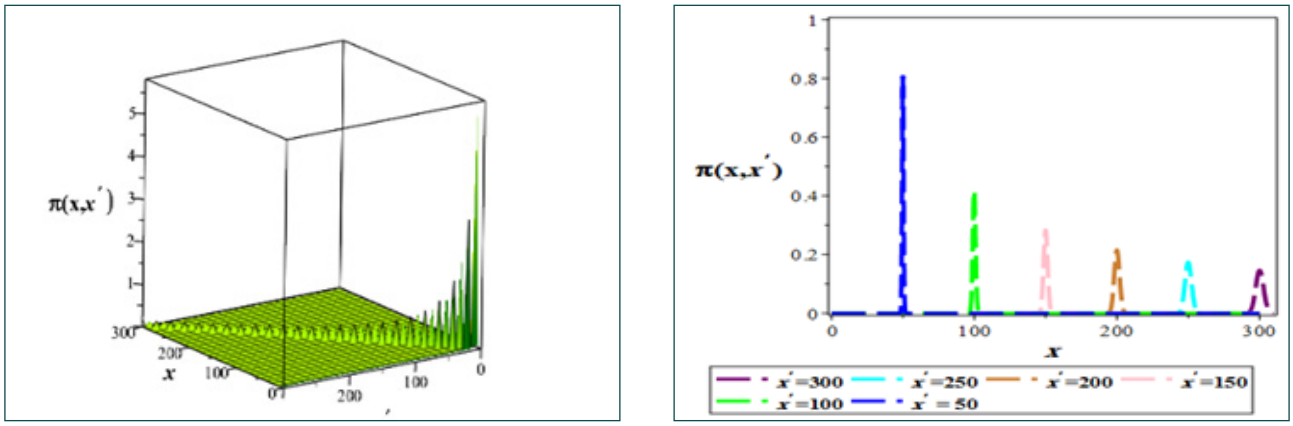

Figure 13: Variations of effective depth versus the actually penetrated depth x and effective penetrated depth x´

precise. Eq. (34) is constructed to fit the experimental results. We observe a great agreement for the range of protons in liquid water. We have therefore obtained an explanation for the passage of protons through the matter which reproduces accurately the results from Monte Carlo simulations. In order to further address the physics behind the Bragg peak features, we now analyze the individual contribution of the different inelastic processes to the depth-dose curve. For a typical proton beam with an initial kinetic energy of 100 MeV, it is observed that if we neglect stripping, charge transfer, and also hydrogen ionization terms, the change produced in the position of the peak is lower than 1 mm; a negligible distance. In addition, the linear energy transfer deposited in the peak is reduced to around 0.005%. If only the excitation term is removed and the other contributions are all kept, we observe a shift in the position of the peak of around 1.5 mm, whereas the change in the amount of energy deposited per unit length is negligible. Finally, removing just proton ionization makes the Bragg peak vanish. This shows that, from all the physical processes taking place in this situation, only proton ionization and excitation (the latter on a smaller scale) contribute to the properties of the Bragg peak. Thus, the other terms, affecting only low energies, produce together solely a very small variation in the height and width of the peak. To improve this work, the authors of this article advise the readers of this article, in order to more accurately estimate the side effects in proton therapy, the use of PMMA biomaterial instead of water in Monte Carlo simulation is preferred.

6-Conclousion

In proton radiotherapy, protons interact with matter in three ways: i) Multiple collisions with atomic electrons cause them to lose energy and eventually stop. ii) Multiple collisions with atomic nuclei cause them to scatter by a few degrees. iii) Occasional hard scatters by nuclei or their constituents throw a dose out to large distances from the beam. Unlike the first two processes, these hard scatters or 'nuclear interactions' do not obey any simple theory, but they are rare enough to be treated as a correction. All three interactions combine in the Bragg curve, the depth-dose distribution of a mono-energetic beam stopping in water, and the signature property of charged radiotherapy beams. In this research, for the first time, we have considered comprehensive physical processes in detail that can affect the proton beam radiation in water, which can help cancer treatment. Using these different processes, we can determine the absorbed dose deposited, the different effects contributing to the total stopping cross section, including ionization and excitation of the medium, charge transfer, stripping, and ionization by the neutral projectile in a water phantom. Our obtained results show that, since straggling dominates the Bragg peak, and is a constant fraction of the range, it follows that Bragg peaks taken at lower energies are sharper.

Acknowledgments

This work is supported by the Islamic Azad University of Shiraz.

References:

1. Miller KD, Nogueira L, Mariotto AB, et al. Cancer treatment and survivorship statistics, 2019. CA: A Cancer Journal for Clinicians. 2019;69:363–385.
2. Borras JM, Lievens Y, Barton M, et al. How many new cancer patients in Europe will require radiotherapy by 2025? An estro-hero analysis. Radiotherapy & Oncology. 2016;119:5–11.
3. Baskar R, Lee KA, Yeo R, et al. Cancer and radiation therapy: current advances and future directions. International Journal of Medical Sciences. 2012;9:193.
4. Younkin J, Bues M, Sio T, et al. Multiple energy extraction reduces beam delivery time for a synchrotron-based proton spot-scanning system. Advances in Radiation Oncology. 2018;3:412–420.
5. Shen J, Taylor P, Vargas C, et al. The status and challenges forprostate stereotactic body radiation therapy treatments in united states proton therapy centers: an NRG oncology practice survey.International Journal of Particle Therapy. 2024;11:100020.
6. Rwigema J-CM, Langendijk JA, van der Laan HP, et al. A model-based approach to predict short-term toxicity benefits with proton therapy for oropharyngeal cancer. International Journal of Radiation Oncology, Biology, Physics. 2019;104:553–562.
7. Blanchard P, Wong AJ, Gunn GB, et al. Toward a model-based patient selection strategy for proton therapy: external validation of photon-derived normal tissue complication probability mod-els in a head and neck proton therapy cohort. Radiotherapy & Oncology. 2016;121:381–386.
8. Blanchard P, Garden AS, Gunn GB, et al. Intensity-modulated proton beam therapy (IMPT) versus intensity-modulated photon therapy (IMRT) for patients with oropharynx cancer – a case matched analysis. Radiotherapy & Oncology. 2016;120:48–55.
9. Water TA, Bijl HP, Schilstra C, et al. The potential benefit of radiotherapy with protons in head and neck cancer with respect to normal tissue sparing: a systematic review of literature. The Oncologist. 2011;16:366–377.
10. Lin A, Swisher-McClure S, Millar LB, et al. Proton therapy for head and neck cancer: current applications and future directions.Translational Cancer Research. 2012;1(4).
11. Liu W, Zhang X, Li Y, et al. Robust optimization of intensity modulated proton therapy. Medical Physics. 2012;39:1079–1091.
12. Liu W, Frank SJ, Li X, et al. PTV-based IMPT optimization incorporating planning risk volumes vs robust optimization.Medical Physics. 2013;40:021709.
13. Chiang J, Nathan Y, Daniels T, et al. Proton beam radiotherapy for patients with early-stage and advanced lung cancer: a narrative review with contemporary clinical recommendations.Journal of Thoracic Disease. 2021;13:1270.
14. Paganetti H, Niemierko A, Ancukiewicz M, et al. Relative biological effectiveness (RBE) values for proton beam therapy.International Journal of Radiation Oncology, Biology, Physics. 2002;53:407–421.
15. Unkelbach J, Botas P, Giantsoudi D, et al. Reoptimization of intensity modulated proton therapy plans based on linear energy transfer. International Journal of Radiation Oncology, Biology,Physics. 2016;96:1097–1106.
16. Paganetti H, Simone II CB, Bosch W, et al. NRG oncology white paper on the relative biological effectiveness in proton therapy. International Journal of Radiation Oncology, Biology,Physics. 2025;121(1):202–217.
17. Wang L, Wang X, Li Y, et al. Human papillomavirus status and the relative biological effectiveness of proton radiotherapy in head and neck cancer cells. Head & Neck. 2017;39:708–715.
18. Wang L, Fossati P, Paganetti H, et al. The biological basis for enhanced effects of proton radiation therapy relative to photon radiation therapy for head and neck squamous cell carcinoma. International Journal of Particle Therapy. 2021;8:3–13.
19. Yepes P, Adair A, Frank SJ, et al. Fixed-versus variable-RBE computations for intensity modulated proton therapy. Advances in Radiation Oncology.

2019;4:156–167.
20. Von Sonntag C. The chemical basis of radiation biology. Taylor & Francis, London, New York, 1987.
21. Molière G. Theorie der streuung schneller geladenen teilchen II mehrfach-und vielfachstreuung. Z Naturforschg (1948) 3a:78–97.
22. Lewis HW. Multiple scattering in an infinite medium. Phys Rev (1950) 78(5):526–9. doi:10.1103/PhysRev.78.526
23. Highland VL. Some practical remarks on multiple scattering. Nucl Instrum Methods (1975) 129:497–9. doi:10.1016/0029-554X(75)90743-0
24. Gottschalk B. On the scattering power of radiotherapy protons. Med Phys (2010) 37(1):352–67. doi:10.1118/1.3264177
25. Cao W, Khabazian A, Yepes PP, et al. Linear energy transfer incorporated intensity modulated proton therapy optimization.Physics in Medicine and Biology. 2017;63:015013.
26. Niemierko A, Schuemann J, Niyazi M, et al. Brain necrosis in adult patients after proton therapy: is there evidence for dependency on linear energy transfer? International Journal of Radiation Oncology Biology Physics. 2021;109:109–119.
27. Gentile MS, Yeap BY, Paganetti H, et al. Brainstem injury in pediatric patients with posterior fossa tumors treated with proton beam therapy and associated dosimetric factors. International Journal of Radiation Oncology, Biology, Physics. 2018;100:719–729.
28. Peeler CR, Mirkovic D, Titt U, et al. Clinical evidence of variable proton biological effectiveness in pediatric patients treated for ependymoma. Radiotherapy & Oncology. 2016;121:395–401.
29. Underwood TS, Grassberger C, Bass R, et al. Asymptomatic late-phase radiographic changes among chest-wall patients are associated with a proton RBE exceeding 1.1. International Journal of Radiation Oncology, Biology, Physics. 2018;101:809–819.
30. Bolsi A, Placidi L, Pica A, et al. Pencil beam scanning proton therapy for the treatment of craniopharyngioma complicated with radiation-induced cerebral vasculopathies: a dosimetric and linear energy transfer (LET) evaluation. Radiotherapy & Oncology. 2020;149:197–204.
31. Ödén J, Toma-Dasu I, Witt Nyström P, et al. Spatial correlation of linear energy transfer and relative biological effectiveness with suspected treatment-related toxicities following proton therapy for intracranial tumors. Medical Physics. 2020;47:342–351.
32. Eulitz J, Lutz B, Wohlfahrt P, et al. A Monte Carlo based radiation response modelling framework to assess variability of clinical RBE in proton therapy. Physics in Medicine and Biology. 2019;64:225020.
33. Bauer J, Bahn E, Harrabi S, et al. How can scanned proton beam treatment planning for low-grade glioma cope with increased distal RBE and locally increased radiosensitivity for late MR-detected brain lesions? Medical Physics. 2021;48:1497–1507.
34. Bahn E, Bauer J, Harrabi S, et al. Late contrast enhancing brain lesions in proton-treated patients with low-grade glioma: clinical evidence for increased periventricular sensitivity and variable RBE. International Journal of Radiation Oncology Biology Physics. 2020;107:571–578.
35. Marteinsdottir M, Wang C-C, McNamara AL, et al. The impact of variable RBE in proton therapy for left-sided breast cancer when estimating normal tissue complications in the heart and lung. Physics in Medicine and Biology. 2021;66(3):035023.
36. Zhang YY, Huo WL, Goldberg SI, et al. Brain-specific relative biological effectiveness of protons based on long-term outcome of patients with nasopharyngeal carcinoma. International Jour-nal of Radiation Oncology Biology Physics. 2021;110:984–992.
37. Engeseth GM, He R, Mirkovic D, et al. Mixed effect modeling of dose and linear energy transfer correlations with brain image changes after intensity modulated proton therapy for skull base head and neck cancer. International Journal of Radiation Oncology Biology Physics. 2021;111:684–692.
38. Garbacz M, Cordoni FG, Durante M, et al. Study of relationship between dose, LET and the risk of brain necrosis after proton therapy for skull base tumors. Radiotherapy & Oncology.2021;163:143–149.

39. Wang CC, McNamara AL, Shin J, et al. End-of-range radiobiological effect on rib fractures in patients receiving
proton therapy for breast cancer. International Journal of Radiation Oncology Biology Physics. 2020;107:449–454.
40. Yang Y, Vargas CE, Bhangoo RS, et al. Exploratory investigation of dose-linear energy transfer (LET) volume histogram (DLVH) for adverse events study in intensity modulated proton therapy (IMPT). International Journal of Radiation Oncology Biology Physics. 2021;110:1189–1199.
41. Yang Y, Muller OM, Shiraishi S, et al. Empirical relative biological effectiveness (RBE) for osteoradionecrosis (ORN) at the mandible in head and neck cancer patients treated with intensity modulated proton therapy (IMPT): a multicenter, retrospective, cohort study. Frontiers in Oncology. 2022;12:843175.
42. Yang Y, Patel SH, Bridhikitti J, et al. Exploratory study of seed spots analysis to characterize dose and linear-energy-transfer effect in adverse event initialization of pencil-beam-scanning proton therapy. Medical Physics. 2022;49:6237–6252.
43. Bertolet A, Abolfath R, Carlson DJ, et al. Correlation of LET with MRI changes in brain and potential implications for normal tissue complication probability for patients with meningioma treated with pencil beam scanning proton therapy. International Journal of Radiation Oncology, Biology, Physics. 2022;112:237–246.
44. Wilkens J, Oelfke U. A phenomenological model for the relative biological effectiveness in therapeutic proton beams.Physics in Medicine and Biology. 2004;49:2811.
45. Carabe A, Moteabbed M, Depauw N, et al. Range uncertainty in proton therapy due to variable biological effectiveness. Physics in Medicine and Biology. 2012;57:1159–1172.
46. Wedenberg M, Lind BK, Hårdemark B. A model for the relative biological effectiveness of protons: the tissue specific parameter a/b of photons is a predictor for the sensitivity to LET changes.Acta Oncologica. 2013;52:580–588.
47. McNamara AL, Schuemann J, Paganetti H. A phenomenolog-ical relative biological effectiveness (RBE) model for proton therapy based on all published in vitro cell survival data. Physics in Medicine and Biology. 2015;60:8399–8416.
48. Hawkins RB. A microdosimetric-kinetic model for the effect of non-poisson distribution of lethal lesions on the variation of RBE with LET. Radiation Research. 2003;160:61–69.
49. Schulz-Ertner D, Karger CP, Feuerhake A, et al. Effectiveness of carbon ion radiotherapy in the treatment of skull-base chordomas. International Journal of Radiation Oncology, Biol-ogy, Physics. 2007;68:449–457.
50. Elsässer T, Scholz M. Cluster effects within the local effect model. Radiation Research. 2007;167:319–329.
51. Elsässer T, Krämer M, Scholz M. Accuracy of the local effect model for the prediction of biologic effects of carbon ion beams in vitro and in vivo. International Journal of Radiation Oncology, Biology, Physics. 2008;71:866–872.
52. Elsässer T, Weyrather WK, Friedrich T, et al. Quantification of the relative biological effectiveness for ion beam radiotherapy:direct experimental comparison of proton and carbon ion beams and a novel approach for treatment planning. International Journal of Radiation Oncology, Biology, Physics. 2010;78:1177–1183.
53. Carlson DJ, Stewart RD, Semenenko VA, et al. Combined use of Monte Carlo DNA damage simulations and deterministic repair models to examine putative mechanisms of cell killing.Radiation Research. 2008;169:447–459.
54. Stewart RD, Carlson DJ, Butkus MP, et al. A comparison of mechanism-inspired models for particle relative biological effectiveness (RBE). Medical Physics. 2018;45:e925–e952.
55. Paganetti H. Mechanisms and review of clinical evidence of variations in relative biological effectiveness in proton therapy.International Journal of Radi-

ation Oncology, Biology, Physics.2022;112:222–236.
56. Machtay M, Moughan J, Trotti A, et al. Factors associated with severe late toxicity after concurrent chemoradiation for locally advanced head and neck cancer: an RTOG analysis. Journal of Clinical Oncology: Official Journal of the American Society of Clinical Oncology. 2008;26:3582–3589.
57. Dornfeld K, Simmons JR, Karnell L, et al. Radiation doses to structures within and adjacent to the larynx are correlated with long-term diet- and speech-related quality of life. International Journal of Radiation Oncology Biology Physics. 2007;68:750–757.
58. Eisbruch A, Schwartz M, Rasch C, et al. Dysphagia and aspiration after chemoradiotherapy for head-and-neck cancer: which anatomic structures are affected and can they be spared by IMRT? International Journal of Radiation Oncology Biology Physics. 2004;60:1425–1439.